ADVANCED INTELLIGENT SYSTEMS Open Access
www.advintellsyst.com

Self-Powered Smart Vibration Absorber for In Situ Sensing and Energy Harvesting

*Jiawen Xu, Zhenyu Wang, Heng-Yong Nie, Yen Wei, and Yu Liu**

Vibration signals are essential data for the health monitoring of structures and the cyber–physical system. However, commercial vibration sensors are generally installed on struts/surfaces to gather raw data, which affects the result or causes the detachment problem. This study uses a facile 3D printing method to fabricate a smart vibration absorber with an interior multifunctional multimaterial elastic lattice (MMEL). These lattices, which work as vibration absorbers, have been demonstrated to possess the functions of self-powered sensing and energy harvesting via the triboelectric effect. The triangular geometry parameter, materials type, etc. have been investigated to illustrate their basic mechanical and triboelectric properties and their coupled influence. Further, the results of the shock test show that MMEL can decrease the peak force from approximately 625 to 90 N and convey the V_{oc} impulse signal simultaneously. The vibration signal has been collected through the MMEL to detect the vibration frequency and charge a watch simultaneously, demonstrating the feasibility and practical potential of the MMEL. The research provides a new method for constructing a multifunctional vibration absorber for applications.

1. Introduction

Vibration, one of the most common physical phenomena, must be detected or eliminated in applications such as automotives, aerospace, and transportation.[1–8] Nevertheless, detecting the device status via vibration often requires attaching individual sensor modules, such as accelerometer-based, resistive,[9–11] capacitive,[12,13] and optical[14,15] vibration sensors, to the object or structure. During its working period, the sensor encounters a problem when the bonding interface gradually breaks under harsh environments and continuous vibration. In addition, a larger scale, distributed, and expensive sensing system, including the battery, fixture, and so on, results in high maintenance cost, environmental pollution, low robustness, and other issues.

Recently, some studies have been performed on applying soft functional materials to fabricate self-sensing elastic foam or structures. For instance, elastomers that are mixed or coated with conductive filler like carbon black,[16,17] carbon nanotube,[18–20] graphene,[21,22] and metal particles[23,24] have been developed to fabricate sensing function devices in which resistance, capacitance, etc. are monitored. However, the hysteresis of the resistance measurement is inevitable due to the contact and the tunneling effect in the conductive path of the composite,[25,26] especially in its dynamic response. Another method that utilizes the triboelectric effect (TE),[27–29] by establishing contact or friction between the surfaces of materials to change the charge distribution and potential on the surface, improves the performance of the devices using this method in real-time situations.[30–33] Most TE-based devices comprise the following parts: surfaces to be contacted for transferring electrons, electrodes for inducing electrical potential and connecting wires. These parts are in the form of membranes or films that require assembly processes, including binding, cutting, weaving, and so on, before being used in practical applications.[32,34–39] Lately, with the popularization of 3D printing technology, TE devices can be printed to fabricate highly complex 3D structures.[40–43] For example, Chen et al. developed a porous, elastic, and sustainable 3D-printed triboelectric nanogenerator (TENG).[44] Barri et al. fabricated a TENG lattice for sensing and energy harvesting in civil engineering and medical fields.[45,46] Wang et al. combined the processes of assembly and 3D printing to prepare an ultraflexible 3D TENG.[41] Among those 3D printing methods, direct ink writing (DIW) is a novel, simple, compatible 3D printing method based on extrusion and

J. Xu, Z. Wang, Y. Liu
School of Mechanical Engineering
Jiangnan University
Wuxi 214122, P. R. China
E-mail: yuliu@jiangnan.edu.cn

J. Xu, H.-Y. Nie
Surface Science Western
University of Western Ontario
999 Collip Circle, London, Ontario N6G 0J3, Canada

H.-Y. Nie
Department of Physics and Astronomy
The University of Western Ontario
1151 Richmond St, London, Ontario N6A 3K7, Canada

Y. Wei
Department of Chemistry
Tsinghua University
Beijing 100084, P. R. China

The ORCID identification number(s) for the author(s) of this article can be found under https://doi.org/10.1002/aisy.202300792.

DOI: 10.1002/aisy.202300792

filament deposition, which is most suitable for non-Newtonian, high viscosity, functional ink.[47–49]

In this study, we developed a simple one-pass multimaterial DIW printing method to fabricate a novel, silicone-type, multi-functional multimaterial elastic lattice (MMEL), an excellent vibration absorber with multiple functions. As depicted in **Figure 1**a,c, the multimaterial filaments were made from conductive (black) and dielectric (gray) silicone using a microfluidic printhead driven by digitally controlled pneumatic pressure. The single unit shape (Figure 1b) was simplified into a diamond shape and horizontal crossbeam, which are the conductive and dielectric parts. These units were arranged periodically and connected by endpoints to form a mutually conductive triangular lattice structure. The whole structure (or MMEL) was printed according to a custom G-code, which defined the path process and the switching of materials (Figure S10, Supporting Information). Under imposed vibration, the MMEL worked in the single-electrode contact-separation mode[44] when charges were transferred via friction between the conductive and dielectric silicone surfaces. This configuration enabled the MMEL to exhibit excellent mechanical stability, vibration absorbing/sensing ability, and energy harvesting functions. Investigations were done on the antishock and vibration frequency detection abilities of the MMEL, where our device was compared with commercial sensors to prove its equivalent, valuable performance. Our results showed that the smart vibration absorber developed in this study is highly promising for its application in intelligent sports protection or other fields that require shock absorption.

2. Results and Discussion

The smart vibration absorber features an interior multimaterial triangular architecture. Our study delves into these absorbers' mechanical and triboelectric performance by analyzing their 3D elastic structure via experiments and simulation methods.

2.1. Mechanical and Triboelectric Performance

The topology of the structure plays a crucial role in the mechanical and triboelectric performance of the absorbers. Valuable reports that have discussed 3D-printed honeycomb designs[50,51] are available in the literature. Hence, we have compared typical shapes, such as hexagons, quadrilaterals, and triangular lattices, by mechanical simulations (Figure S5, S6, Supporting Information). Then, the triangular lattice, which has a straight and easily controllable deformation (via angle), was chosen to investigate the absorber's mechanical and triboelectric properties and their coupled influence.

As shown in **Figure 2**a, three types of MMELs were fabricated, with variable angles of $\theta = \pi/6$, $\pi/4$, and $\pi/3$, when the other geometric parameters were maintained to be as consistent as possible. The length, L, of one side of the diamond-shaped structure was measured to be 3 mm, and its line width, d, was 0.3 mm, with each type of MMEL containing 5×5 ($M \times N$) units. The conductive parts were made of conductive silicone (denoted as Mat. A) by blending carbon black and polydimethylsiloxane (Sylgard 184). In contrast, the dielectric parts were made of dielectric SE1700 silicone (denoted as Mat. B). As illustrated in Figure 2b,c, compressive vibration experiments were conducted on the samples at 0, 0.25, and 0.7 strains, respectively. Notably, the lattice with $\theta = \pi/4$ and $\pi/3$ underwent apparent buckling, whereas slight buckling was observed in the sample with $\theta =$ of $\pi/6$ (dynamic process in Video S1, Supporting Information).

The strain–stress compression results of the three MMELs are shown in Figure 2d. There is no apparent difference when the strain is under 0.4, thus indicating their low stiffness in the early

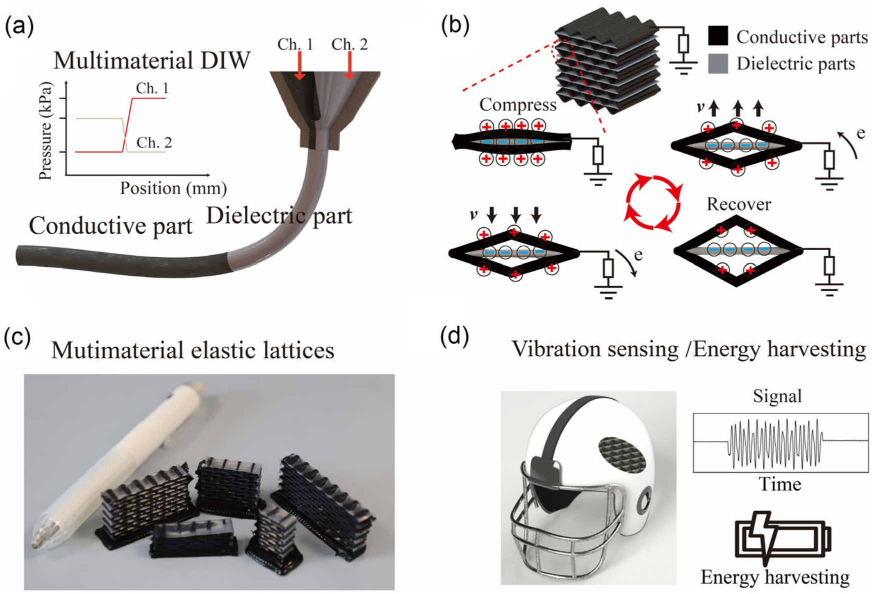

Figure 1. a) Schematic of the multimaterials printing that completes one-pass materials switching; b) working principle of the MMEL under the single electrode mode; c) photographs showing the samples of MMELs; and d) schematic of the application of MMELs in a smart sports protection helmet and energy harvesting.

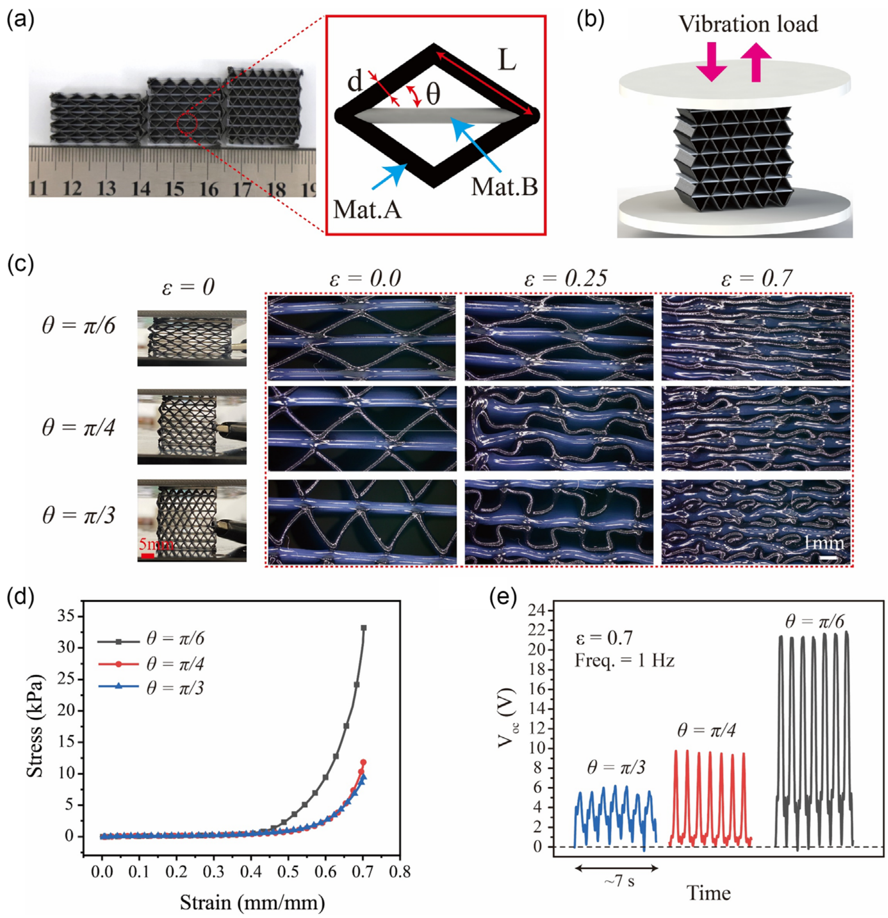

Figure 2. a) Photograph of the MMELs and a schematic of the parameters that define a single unit; b) schematic of the experiment setup; c) internal deformation of the MMELs under compression at strains of 0, 0.25, and 0.7; d) stress–strain curves of quasistatic compression of the MMELs with a load velocity of 5 mm min^{-1}; and e) open-circuit voltage (V_{oc}) output of the lattice subjected to 1 Hz vibration with strains between 0 and 0.7.

stage because the large pore size is suitable for vibration or anti-shock situations. When the strain increases to 0.45, the stress of the MMEL with $\theta = \pi/6$ rises more rapidly than those with $\theta = \pi/4$ and $\pi/3$, which is consistent with the buckling situation. Thus, it can be concluded that the MMEL with $\theta = \pi/6$ quickly enters the densification state compared to the others, which is consistent with the simulation results (Figure S6 and S7, Supporting Information). As shown in Figure 2e, it is evident that different deformation responses of the MMELs result in different open-circuit voltages (V_{oc}) under 1 Hz cyclic loading strain between 0 and 0.7, with the dynamic process shown in Video S2, Supporting Information. The peak values of V_{oc} are approximately 6, 10, and 21 V for the MMELs with $\theta = \pi/3$, $\pi/4$, and $\pi/6$, respectively. This is because the folding of the surface dissipates the external strains and reduces the frictional contact area, thus producing different electrical signals during vibration.

It is well known that the TE hinges on the charge transfer occurring at the two surfaces that are in contact. Consequently, surface properties such as the materials' intrinsic structure and morphology play a critical role in the performance of the materials in generating the TE. Thus, three types of constructing materials were considered in this study: conductive silicone (Mat. A in Figure 2a), dielectric silicone (Mat. B in Figure 2a), and a type of dielectric silicone (denoted as Mat. C) mixed with dibutyl phthalate (DBP). The detailed formulation and preparation of these materials have been given in the Experimental Section. In particular, DBP was taken as the liquid pore-forming agent for producing a rough surface by performing the following steps: DBP was first dispersed into the silicone matrix via vigorous mechanical stirring to form a uniform distribution in the form of droplets. Subsequently, the cured printed sample underwent multiple immersion cycles in deionized (DI) water to dissolve and remove the DBP droplets to obtain the final porous surface. As shown in **Figure 3**a, Mat. A exhibits uniform submicron structures attributed to the carbon black nanoparticle—similarly, the surface of Mat. C has large micropores and a rough surface resulting from the DBP microdroplet after soaking in DI water. Without any other additive, Mat. B showed a smoother and neater surface compared to Mat. A and Mat. C. Next, three types of MMELs, composed of different material combinations, were printed while still maintaining the same size parameters (i.e., $\theta = \pi/3$, $L = 3$ mm, $d = 0.3$ mm, $M \times N = 5 \times 5$ units and the same thickness of 6 mm along the stacking direction) with their combinations denoted as

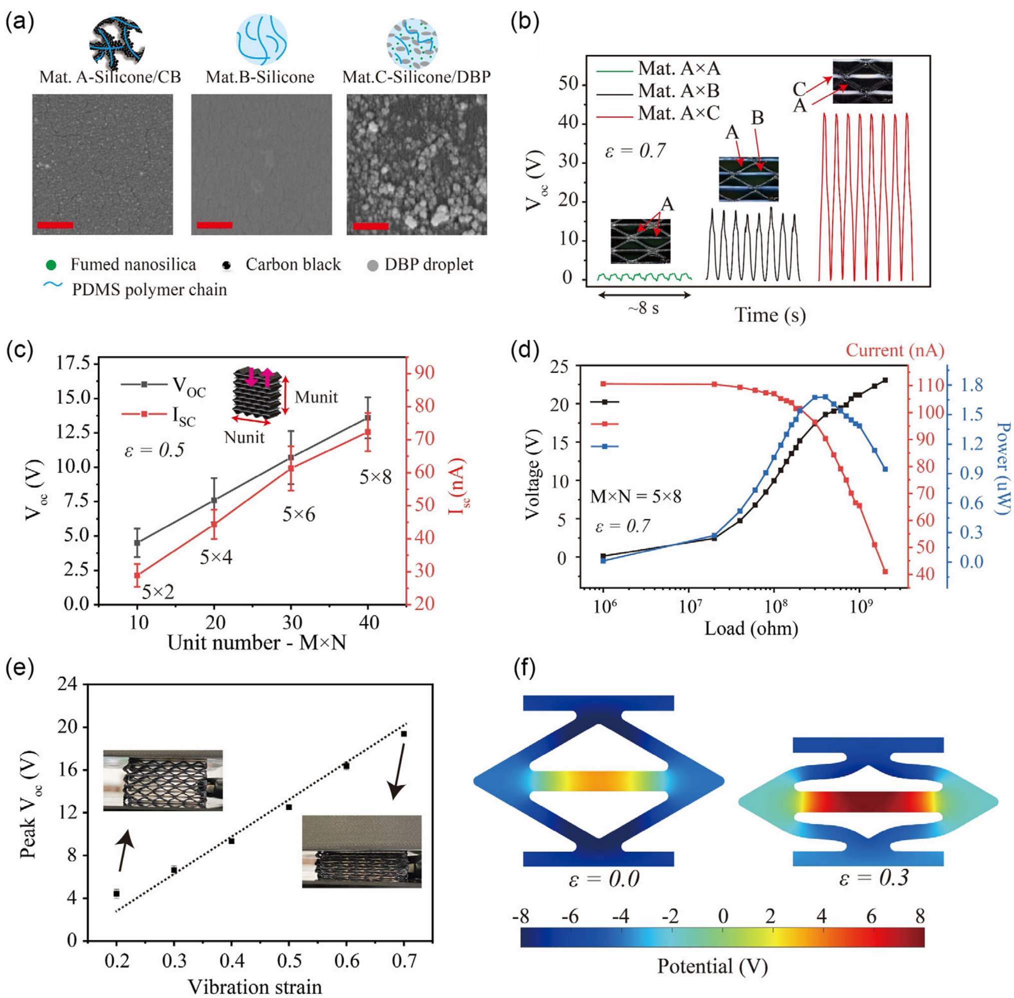

Figure 3. Triboelectric performance of the samples with all tests conducted under 1 Hz vibration and the topological parameters of the samples fixed to, i.e., $\theta = \pi/3$, $L = 3$ mm, and $d = 0.3$ mm: a) SEM images of the surfaces of the materials and schematics of the ink components (uncured). The scale bar is 200 nm; b) open-circuit voltage (V_{oc}) for the MMELs with different materials combinations under 1 Hz vibration and its strain between 0 and 0.7; c) peak open-circuit voltage and short-circuit current (I_{sc}) as a function of the unit numbers of the MMEL; d) output voltage, present, and powers of MMELs with 40 units; e) V_{oc} of an MMEL as a function of the vibration strain; and f) simulated electrical potential fields at stains of 0 and 0.3.

$A \times A$ (the control group), $A \times B$, and $A \times C$. Subsequently, these structures were subjected to a 1 Hz vibration under a strain of 0.5 to measure their V_{oc}. Figure 3b shows that the lattices exhibit a distinct situation where Mat. $A \times C$ has the highest V_{oc} output of approximately 40 V. Surprisingly, the lattice within the Mat. $A \times A$ combination produces a nonzero signal. Thus, it was inferred that the TE would occur between the carbon black nanoparticle and the silicone matrix at the microscopic scale as expected from the atomic force microscopy (AFM) results, including the sample's topography and phase shift image (Figure S8, Supporting Information).

As the lattice structure primarily consists of periodical single units, the number of units can influence the electrical output. As shown in Figure 3C, the lattices with various numbers of units ($5 \times N$, where $N = 2$, 4, 6, and 8) were subjected to 1 Hz vibration strain between 0 and 0.5. As the number of units increased, V_{oc} and I_{sc} exhibited an almost linear relationship with a slope of approximately 0.25 V unit^{-1} and 15 nA unit^{-1}, respectively. This is because these units are connected in series electrically using conductive nodes (Figure S10, Supporting Information), and due to the excellent conductivity of Mat. A,[52,53] the MMEL with more units offers a larger contact surface for tribo-electrification, thus increasing the total charges and the values of V_{oc}, I_{sc}. To evaluate its potential as a power source, the output of a lattice of 40 units, i.e., V, I, and P, was tested with various external resistances under a 1 Hz vibration strain between 0 and 0.7. As can be seen from Figure 3d, the measured V_{oc}, I_{sc}, and the corresponding output power peak at an external load of approximately 300 MΩ. Moreover, the output of V_{oc} increases linearly with 1 Hz vibration strain under continuous cyclic compression because a larger contact area has a higher compressive strain, according to analysis in the previous subsection. To further understand the TE effect during vibration, a simulation (Figure 3f and S1, Supporting Information) was performed to understand the electric potential distribution under the vibration at a strain of 0 and 0.3.

2.2. Applications

Given the validation of self-powered sensing and mechanical performance of the fabricated MMELs, several practicable applications of MMELs have the potential to serve as smart vibration absorbers for shock mitigating/monitoring and energy harvesting. Simple shock experiments with or without the cushion MMEL were conducted to demonstrate this. The MMEL was printed in a cubic structure of 23 mm length, 11 mm width, and 17.8 mm height. As shown in **Figure 4**a, a custom-built apparatus was utilized, which dropped a steel hammer from different heights to give the impulse, and the resultant force was recorded. As expected, the MMEL provided a significant cushioning effect and decreased the peak force during the impact. As shown in Figure 4b, the MMEL extended the duration of interaction between the hammer and the base from ≈5 to ≈20 ms and eliminated the subsequent high-frequency vibration. The corresponding one-shot triboelectric signals were acquired during this experiment, which exhibited similar waveforms recorded by the rigid force sensor (Video S3, Supporting Information). Following this, the sample was arranged as a smart foam within a miniature rugby helmet for shock detection, and the helmet was punched to simulate violent collisions in courts. As shown in Figure 4d, the hamlet could record the electric signals of each punch as raw data to analyze the motion status of the athlete.

In addition to their use in shock detection, the output signals of MMELs from continuous mechanical vibration can also be used as a frequency detector. As an example, an MMEL was used to measure the motion frequency of a fascial massager gun at different gear levels by measuring the I_{sc} value as shown in **Figure 5**, where the sample has 4×5 units with $\theta = \pi/6$, 30 mm length, 17.64 mm height, and 6 mm width. The vibration frequency was obtained from the discrete Fourier transform (DFT) analysis of I_{sc}, which was collected at a high sampling rate of 1 kHz (Figure 5b). The frequency domain analysis showed that the frequency gradually increased from 25 to 36 Hz when the gears were switched from 1 to 6, further proved by another commercial laser velocimeter (Figure 5c). As shown in Figure 5d and the results of the durability test (Figure S5, Supporting Information), it was confirmed that the MMEL could convert mechanical energy to electrical energy under long-term vibration through a bridge circuit and stored energy in a 10 μF capacitor. After charging for 5 min, the capacitor could light a microelectronic watch for approximately 3 s, as shown in the inset of Figure 5d or Video S4, Supporting Information. These demonstrations highlight the potential of the MMELs as versatile, smart, soft materials for monitoring and vibration absorption in various applications.

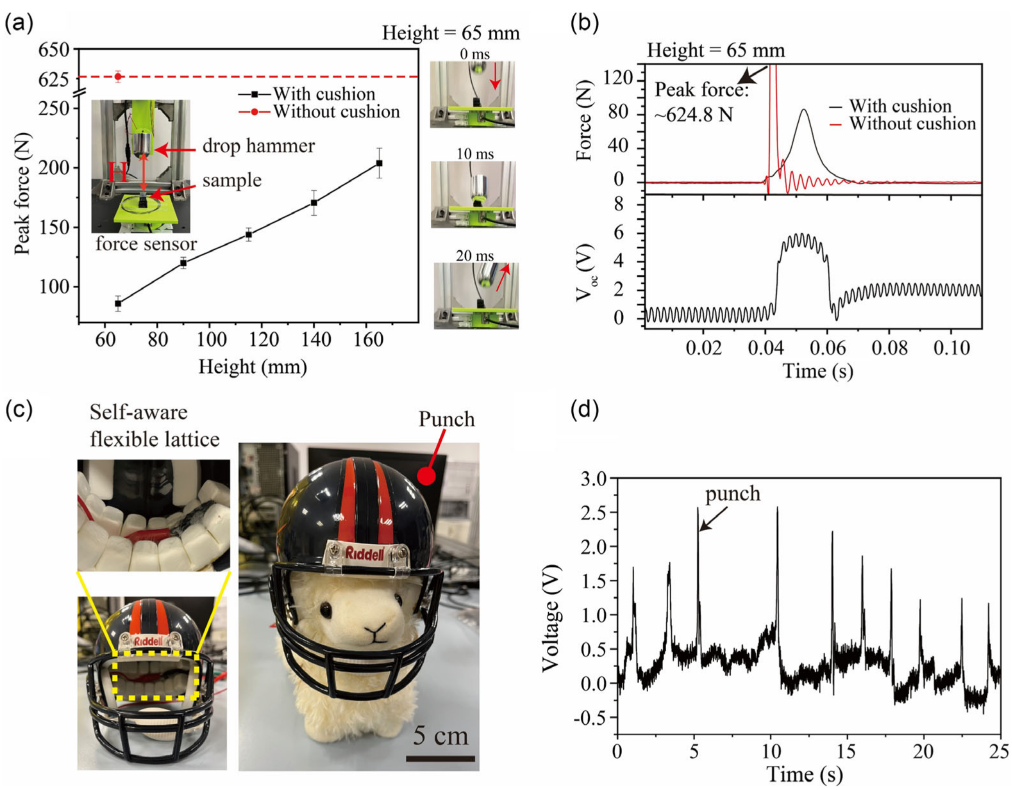

Figure 4. a) The free-fall shock experiments showing the relationship between the peak force and the height of the falling harmer; b) the upper plot shows the displays data captured by the force sensor, whereas the bottom one represents the triboelectric signal from the MMEL; c) the MMEL is integrated into the structure of a rugby helmet as a cushioning component; and d) time history of the output voltage (V_{oc}) that reflects the punching action.

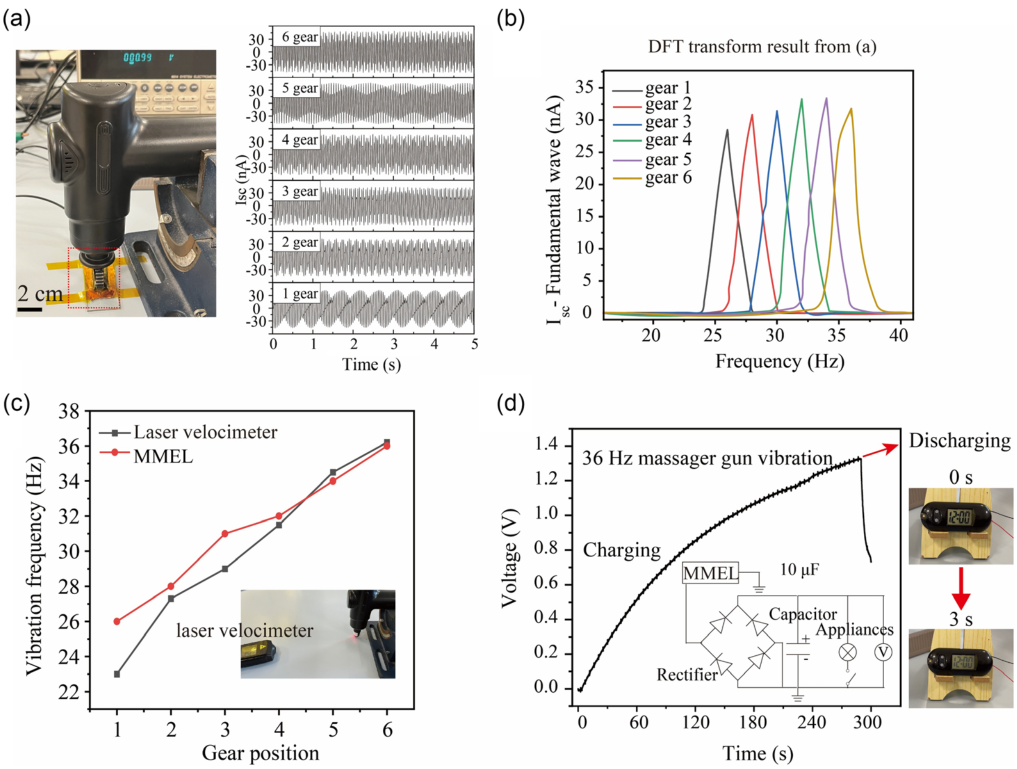

Figure 5. a) (left) Experimental setup for measuring the vibration frequency of a massager gun and (right) short-circuit current (I_{sc}) for 5 s at various gear levels; b) fundamental frequency of I_{sc} in the frequency domain after applying DFT; c) comparison of the vibration frequency test of the laser velocimeter and the MMEL; and d) time history of the charging and discharging voltage for lighting a watch.

3. Conclusion

In summary, we have successfully utilized a simple multimaterial DIW to fabricate a rapid elastic vibration absorber with an interior multimaterial triangular lattice with mechanical robustness and self-powered sensing capabilities. Due to the high flexibility and controllability of 3D printing, we can readily tailor the shape parameters and material types of the MMELs to investigate factors such as the unit geometry parameters, unit number, and material surface via experiments and simulation methods. Interestingly, buckling inside the lattice will delay the densification of MMELs and decrease friction area, eliminating the peak value of the triboelectric outputs. Finally, simple but straightforward demonstrations of using MMELs as shock absorbers, for vibration frequency detection, and for energy harvesting have been conducted and compared with commercial sensors to show their competence, versatility, and advantages. Using the proposed innovative fabrication method and the application examples demonstrated in this study, people can foresee great potential and further applications of MMELs in wearable devices, transportation protection, and Internet of Things in the future.

4. Experimental Section

Materials: The conductive silicone (denoted as Mat. A) included three components: Polydimethylsiloxane (PDMS) prepolymer and cure agent (Sylgard 184, Dow Corning), and carbon black (Super P Li, 50 nm, Guangdong Canrd New Energy Technology Co., Ltd.) at a weight ratio of 10:1:1. Among the dielectric silicones, one (denoted as Mat. B) was prepared by mixing the SE1700 base, the corresponding catalyst (Dow Corning) at a weight ratio of 10:1, and the other (denoted as Mat. C) contained SE1700 base, SE1700 catalyst, PDMS precursor, PDMS cure agent, and dibutyl phthalate (DBP, Sinopharm Chemical Reagent Co., Ltd.) as a foaming agent[54] at a weight ratio of 10:1:10:1:10. Above kinds of uniform inks were obtained by mixing at 2000 rpm for 3 min in a planetary mixer (ZYMC-180V, ZYE Technology Co., Ltd.). All formulated inks were loaded into 30-cc syringes (Nordson, USA) and centrifuged at 5000 rpm for 5 min before printing to remove the existing bubbles.

Characterizations: The rheological properties of the inks were characterized using a stress-controlled rheometer (DHR-2, TA Instruments) with a cone plate fixture. The photographs of the printed samples were captured using an optical microscope (DVM6 A, Leica Microsystems GmbH) or a camera (Canon EOS Mark II, Japan). Compressive mechanical tests were conducted using a universal testing machine (QJ211S, Qingji Co. Ltd., China) with a 5 mm min^{-1} loading speed. A home-built linear motor was used to form controlled vibration, drive the MMEL to contact, and separate for quantified measurement. AFM examined the surface morphology and stiffness (XE-100, Park Systems, Korea) with specific parameters in the Supporting Information. Impact tests were performed using custom-built equipment consisting of a force sensor and dynamic strain collection and analysis system (uT7800, Wuhan Youtai Electronic Technology Co., Ltd.). The electrical properties, such as open-circuit voltage (V_{oc}) and short-circuit current (I_{sc}), were measured using an electrometer (6514, Keithley Instruments, USA) and NI DAQ suit (NI 9205, USA), with a sampling rate of 1 kHz (wire connection in Figure S11, Supporting Information).

Simulation: The extrusion process was simulated using the ANSYS Fluent with multiphase flow modules (Figure S2, Supporting

Information). The multiphysics software COMSOL and its solid mechanical and electrostatics modules (Figure S1, Supporting Information) were utilized to visualize the dynamic process of electrical potential during vibration. Compressive hyperplastic materials (silicone) were simulated using the commercial finite element software ABAQUS. This detailed methodology of simulations can be found in the Supporting Information.

Fabrication of Smart Vibration Absorber: The printer (Formlabs 3, USA) fabricated the printhead using High Temp V2 resin. The dimensions and morphology of the printhead are presented in Figure S3, Supporting Information, noting that the outlet diameter is 0.3 mm. After centrifugation, the printed ink was loaded into a 30-cc syringe and then connected to the printhead through the Luer fittings. The customized printer can be programmed to recognize G-codes containing printing speed, extrusion pressure, and path information. The G-codes were generated using MATLAB script and executed through the LabVIEW interface according to the design path (Figure S10, Supporting Information). Fluorinated glass slides with incompatible interfaces were used as the printing substrate; then, printed samples were cured in an oven at 120 °C for 2 h.

Supporting Information

Supporting Information is available from the Wiley Online Library or from the author.

Acknowledgements

The authors acknowledge the fundings from the National Natural Science Foundation of China (grant nos. 51875253 and 52175201), Jiangsu Provincial Key Research and Development Program (grant no. BE2022069-2), and China Scholarship Council (grant no. 202206790068).

Conflict of Interest

The authors declare no conflict of interest.

Author Contributions

J.X.: Conceptualization, methodology, experiments, writing—original draft, data processing; Z.W.: writing—review and editing; H.-Y.N.: writing—review and editing; Y.W.: writing—review and editing; Y.L.: conceptualization, funding acquisition, supervision, writing—review and editing.

Data Availability Statement

The data that support the findings of this study are available from the corresponding author upon reasonable request.

Keywords

3D printing, energy harvesting, multifunctional, self-powered vibration sensing

Received: November 20, 2023
Revised: February 15, 2024
Published online: March 12, 2024

[1] O. Avci, O. Abdeljaber, S. Kiranyaz, M. Hussein, M. Gabbouj, D. J. Inman, *Mech. Syst. Signal Process.* **2021**, *147*, 107077.
[2] J. H. Lee, K. Cho, K. Cho, *Adv. Mater.* **2023**, *35*, 2209673.
[3] Y. S. Li, H. C. Liu, K. Zhou, H. S. Qin, W. S. Yu, Y. L. Liu, *Compos. Struct.* **2022**, *287*, 115335.
[4] P. Abhishek Dhananjay, R. Jegadeeshwaran, *Measurement* **2021**, *173*, 108649.
[5] M. Tiboni, C. Remino, R. Bussola, C. Amici, *Appl. Sci.* **2022**, *12*, 972.
[6] M. I. M. Ismail, R. A. Dziyauddin, N. A. A. Salleh, F. Muhammad-Sukki, N. A. Bani, M. A. M. Izhar, L. A. Latiff, *IEEE Access* **2019**, *7*, 51965.
[7] W. Q. Sheng, H. J. Xiang, Z. W. Zhang, X. P. Yuan, *Compos. Struct.* **2022**, *299*, 116040.
[8] M. P. Arunkumar, J. Pitchaimani, K. V. Gangadharan, M. C. Leninbabu, *Aerosp. Sci. Technol.* **2018**, *78*, 1.
[9] M. Mishra, P. B. Lourenco, G. V. Ramana, *J. Build. Eng.* **2022**, *48*, 103954.
[10] T. Wen, A. Ratner, Y. Jia, Y. Shi, *Compos. Struct.* **2021**, *255*, 112979.
[11] L. Lampani, P. Gaudenzi, *Compos. Struct.* **2018**, *202*, 136.
[12] A. Torkkeli, O. Rusanen, J. Saarilahti, H. Seppä, H. Sipola, J. Hietanen, *Sens. Actuators, A* **2000**, *85*, 116.
[13] S. Lee, J. Kim, I. Yun, G. Y. Bae, D. Kim, S. Park, I.-M. Yi, W. Moon, Y. Chung, K. Cho, *Nat. Commun.* **2019**, *10*, 2468.
[14] M. Neumann, F. Dreier, P. Günther, U. Wilke, A. Fischer, L. Büttner, F. Holzinger, H.-P. Schiffer, J. Czarske, *Mech. Syst. Signal Process.* **2015**, *64*, 337.
[15] S. J. Rothberg, M. Allen, P. Castellini, D. Di Maio, J. Dirckx, D. Ewins, B. J. Halkon, P. Muyshondt, N. Paone, T. Ryan, *Opt. Lasers Eng.* **2017**, *99*, 11.
[16] Z. Wang, X. Guan, H. Huang, H. Wang, W. Lin, Z. Peng, *Adv. Funct. Mater.* **2019**, *29*, 1807569.
[17] W. Zhai, Q. Xia, K. Zhou, X. Yue, M. Ren, G. Zheng, K. Dai, C. Liu, C. Shen, *Chem. Eng. J.* **2019**, *372*, 373.
[18] Q. Chen, J. Zhao, J. Ren, L. Rong, P. F. Cao, R. C. Advincula, *Adv. Funct. Mater.* **2019**, *29*, 1900469.
[19] Q. Chen, P. F. Cao, R. C. Advincula, *Adv. Funct. Mater.* **2018**, *28*, 1800631.
[20] J. Huang, X. Yang, J. Liu, S. C. Her, J. Guo, J. Gu, L. Guan, *Nanotechnology* **2020**, *31*, 335504.
[21] S. Asutkar, M. Korrapati, D. Gupta, S. Tallur, *IEEE Sens. Lett.* **2020**, *4*, 1.
[22] R. Ajith, A. Tewari, D. Gupta, S. Tallur, *IEEE Sens. Lett.* **2017**, *1*, 1.
[23] I. S. Yoon, S. H. Kim, Y. Oh, B. K. Ju, J. M. Hong, *Sci. Rep.* **2020**, *10*, 5036.
[24] I. S. Yoon, Y. Oh, S. H. Kim, J. Choi, Y. Hwang, C. H. Park, B. K. Ju, *Adv. Mater. Technol.* **2019**, *4*, 1900363.
[25] Z. Wang, Q. Zhang, Y. Yue, J. Xu, W. Xu, X. Sun, Y. Chen, J. Jiang, Y. Liu, *Nanotechnology* **2019**, *30*, 345501.
[26] J. Xu, X. Zhang, Y. Liu, Y. Zhang, H.-Y. Nie, G. Zhang, W. Gao, *Addit. Manuf.* **2020**, *36*, 101487.
[27] F.-R. Fan, Z.-Q. Tian, Z. L. Wang, *Nano Energy* **2012**, *1*, 328.
[28] S. Li, D. Liu, Z. Zhao, L. Zhou, X. Yin, X. Li, Y. Gao, C. Zhang, Q. Zhang, J. Wang, Z. L. Wang, *ACS Nano* **2020**, *14*, 2475.
[29] Z. Lin, C. Sun, W. Liu, E. Fan, G. Zhang, X. Tan, Z. Shen, J. Qiu, J. Yang, *Nano Energy* **2021**, *90*, 106366.
[30] S. Chun, W. Son, H. Kim, S. K. Lim, C. Pang, C. Choi, *Nano Lett.* **2019**, *19*, 3305.
[31] L. Wang, W. Liu, Z. Yan, F. Wang, X. Wang, *Adv. Funct. Mater.* **2020**, *31*, 2007221.
[32] H. Tao, J. Gibert, *Adv. Funct. Mater.* **2020**, *30*, 2001720.
[33] Y. C. Qi, G. X. Liu, Y. Y. Gao, T. Z. Bu, X. H. Zhang, C. Q. Xu, Y. Lin, C. Zhang, *ACS Appl. Mater. Interfaces* **2021**, *13*, 26084.
[34] Y. Tong, Z. Feng, J. Kim, J. L. Robertson, X. Jia, B. N. Johnson, *Nano Energy* **2020**, *75*, 104973.
[35] X. Xu, Q. Wu, Y. Pang, Y. Cao, Y. Fang, G. Huang, C. Cao, *Adv. Funct. Mater.* **2021**, *32*, 2107896.

[36] J. Chen, G. Zhu, W. Yang, Q. Jing, P. Bai, Y. Yang, T. C. Hou, Z. L. Wang, *Adv. Mater.* **2013**, *25*, 6094.
[37] J. Chen, Z. L. Wang, *Joule* **2017**, *1*, 480.
[38] S. Niu, Y. Liu, S. Wang, L. Lin, Y. S. Zhou, Y. Hu, Z. L. Wang, *Adv. Funct. Mater.* **2014**, *24*, 3332.
[39] Z. Li, G. Jin, Y. Ma, X. Zhou, Y. Gao, X. Xiong, K. Dong, L. Lyu, *Compos. Struct.* **2023**, *322*, 117430.
[40] Z. Wang, C. Luan, Y. Zhu, G. Liao, J. Liu, X. Li, X. Yao, J. Fu, *Nano Energy* **2021**, *90*, 106534.
[41] B. Chen, W. Tang, T. Jiang, L. Zhu, X. Chen, C. He, L. Xu, H. Guo, P. Lin, D. Li, J. Shao, Z. L. Wang, *Nano Energy* **2018**, *45*, 380.
[42] C. Qian, L. Li, M. Gao, H. Yang, Z. Cai, B. Chen, Z. Xiang, Z. Zhang, Y. Song, *Nano Energy* **2019**, *63*, 103885.
[43] G. Liu, Y. Gao, S. Xu, T. Bu, Y. Xie, C. Xu, H. Zhou, Y. Qi, C. Zhang, *EcoMat* **2021**, *3*, e12130.
[44] S. Chen, T. Huang, H. Zuo, S. Qian, Y. Guo, L. Sun, D. Lei, Q. Wu, B. Zhu, C. He, X. Mo, E. Jeffries, H. Yu, Z. You, *Adv. Funct. Mater.* **2018**, *28*, 1805108.
[45] K. Barri, P. Jiao, Q. Zhang, J. Chen, Z. Lin Wang, A. H. Alavi, *Nano Energy* **2021**, *86*, 106074.
[46] K. Barri, Q. Zhang, J. Kline, W. Lu, J. Luo, Z. Sun, B. E. Taylor, S. G. Sachs, L. Khazanovich, Z. L. Wang, A. H. Alavi, *Adv. Mater.* **2023**, *35*, e2211027.
[47] J. A. Lewis, *Adv. Funct. Mater.* **2006**, *16*, 2193.
[48] A. S. Gladman, E. A. Matsumoto, R. G. Nuzzo, L. Mahadevan, J. A. Lewis, *Nat. Mater.* **2016**, *15*, 413.
[49] R. L. Truby, J. A. Lewis, *Nature* **2016**, *540*, 371.
[50] C. Qi, F. Jiang, S. Yang, *Composites, Part B* **2021**, *227*, 109393.
[51] Y. Zhang, X. Ren, W. Jiang, D. Han, X. Yu Zhang, Y. Pan, Y. Min Xie, *Mater. Des.* **2022**, *221*, 110956.
[52] A. Chortos, J. Mao, J. Mueller, E. Hajiesmaili, J. A. Lewis, D. R. Clarke, *Adv. Funct. Mater.* **2021**, *31*, 2010643.
[53] Y. Zhu, N. Liu, Z. Chen, H. He, Z. Wang, Z. Gu, Y. Chen, J. Mao, Y. Luo, Y. He, *ACS Mater. Lett.* **2023**, *5*, 704.
[54] C. K. Loeb, D. T. Nguyen, T. M. Bryson, E. B. Duoss, T. S. Wilson, J. M. Lenhardt, *Addit. Manuf.* **2022**, *55*, 102837.